Z. Kristallogr. **227** (2012) 84–91 / **DOI** 10.1524/zkri.2012.1432

New insights into the lattice dynamics of α-quartz

Alexei Bosak*,[I], Michael Krisch[I], Dmitry Chernyshov[II], Björn Winkler[III], Victor Milman[IV], Keith Refson[V] and Clemens Schulze-Briese[VI,1]

[I] European Synchrotron Radiation Facility, BP 220, 38043 Grenoble Cedex, France
[II] Swiss-Norwegian Beam Lines, BP 220, 38043 Grenoble Cedex, France
[III] Geowissenschaften, Goethe-Universität, Altenhoeferallee 1, D-60438 Frankfurt a.M., Germany
[IV] Accelrys, 334 Cambridge Science Park, Cambridge CB4 0WN, United Kingdom
[V] Rutherford-Appleton Laboratory, Building R3, Chilton, Didcot, Oxfordshire, OX11 0QX, UK
[VI] Paul Scherrer Institut, Swiss Light Source, 5232 Villigen – PSI Switzerland

Received June 24, 2011; accepted October 21, 2011

α-Quartz / Diffuse scattering / Lattice dynamics / Inelastic scattering / Phonons / Debye-Waller factors

Abstract. The lattice dynamics of α-quartz has been studied in great details by combining inelastic X-ray scattering (IXS) from single- and polycrystalline samples, 3D mapping of thermal diffuse scattering (TDS) and *ab initio* calculations. Pronounced features in TDS patterns have been identified and the origin of first peak in vibrational density of states is unambiguously revealed.

1. Introduction

Quartz, an ubiquitous mineral, has been the focus of many studies, as understanding its structure-property relations is of fundamental importance for numerous technological applications such as pressure gauges, oscillators, resonators, and wave stabilizers making use of the piezoelectric properties. Its optical activity, UV-transparency and hardness are further attractive features. In addition, the acentric structure of α-quartz, which can be described as spirals made up of corner-connected SiO_4-tetrahedra, has intrinsic degrees of freedom, which are the origin of the alpha-incommensurate-beta phase transition [1, 2]. Quartz, and more generally silicates, play an important role in geophysical investigations, since oxygen and silicon are the main constituents of Earth's crust [3]. Silica, the amorphous form of SiO_2, is a prototypical strong glass former, and its low-frequency vibrational dynamics have been intensively studied, since it is intimately linked to the observed low-temperature anomalies of the thermal conductivity. In particular, the origin of the observed excess of vibrational density-of-states $g(\omega)$ (VDOS), the so-called boson peak, is still discussed controversially (see *e.g.* [4, 5] and references therein).

The lattice dynamics of quartz has been extensively studied, including a considerable number of measurements in the proximity of the Γ point by ultrasound techniques [6], Raman [7, 8] and infrared spectroscopy [9] – to mention only a few publications – and extensive investigations of the phonon dispersion in high-symmetry directions based on inelastic neutron scattering (INS) [10, 11] and inelastic X-ray scattering (IXS) [12] have been presented. On the other hand, a full experimental study of the lattice dynamics, including not only phonon dispersion curves, but also phonon eigenvectors for *arbitrary* momentum transfers, is still missing. An impressive study of the phonon eigenvectors of quartz at the M point was performed by INS [13], but in view of the relative complexity of the structure – with 9 atoms per elementary cell and 27 phonon branches – it is unlikely that such a study will be performed for anything but a very limited number of reciprocal lattice points and modes. Ab initio calculations of the phonon dispersion curves of quartz are generally in very good agreement with experimentally observed frequencies. A summary of earlier results has been given by Refson *et al.* (2006) [14], who, in addition to a calculation of dispersion curves, also computed an IR spectrum and commented on the need for highly converged geometry optimisations due to the presence of rigid unit modes. However, in most cases where lattice dynamical models are evaluated, only frequencies are compared, as in only very few cases experimentally determined eigenvectors are available for comparison.

In the following we report results on the successful combination of thermal diffuse scattering and inelastic X-ray scattering from single- and polycrystalline SiO_2 with state-of-the-art *ab initio* calculations. We utilize the validated model to investigate specific aspects of the quartz lattice dynamics (eigenvector analysis, mode character, and anisotropic thermal parameters) and, most importantly, identify the origin of the lowest VDOS singularity. The manuscript is organized as follows: Section II is dedicated to the experimental techniques, Section III introduces the details of the employed calculation, Section IV presents the experiment results and provides the discussion, and Section V presents the conclusions and future trends.

* Correspondence author (e-mail: bossak@esrf.fr)
[1] Current address: DECTRIS Ltd., Neuenhofer Str. 109, 5400 Baden, Switzerland

2. Experimental methods

TDS studies were performed on beamline X06SA at the Swiss Light Source. X-rays were monochromatized to $\lambda = 0.7084$ Å, within a bandwidth of $\Delta\lambda/\lambda \sim 2\times10^{-4}$. A high quality rod-like 1 mm thick α-quartz crystal (mosaic spread $\sim$0.002° FWHM) was mounted on a rotation stage, and diffuse scattering patterns were recorded with a PILATUS 6M pixel detector [15] with an increment of 0.1° over an angular range of 360°. Orientation matrix refinement and preliminary reciprocal space reconstructions were performed using the CrysAlis software package [16]. For the final reciprocal space reconstructions we applied corrections for polarization and for solid angle conversion associated with the planar projection. For 3D visualization purposes the reconstructed volume is averaged with its symmetrically equivalent orientations employing the Laue symmetry of the sample, thus improving the signal-to-noise ratio and removing the gaps between the individual detector elements. Constant-intensity surfaces were traced from the generated 3D data array using the UCSF Chimera package [17] and for presentation purposes rendered with the POV-Ray software [18].

The IXS experiment was performed on beamline ID28 at the European Synchrotron Radiation Facility. The instrument was operated at 17794 eV, providing an overall energy resolution of 3.0 meV full-width-half-maximum (FWHM). Direction and size of the momentum transfer were selected by an appropriate choice of the scattering angle and the crystal orientation in the horizontal scattering plane. The momentum resolution was set to $\sim$0.25 nm^{-1} $\times$ 0.75 nm^{-1} in the horizontal and vertical plane, respectively. Further details of the experimental setup and data treatment procedures can be found elsewhere [19]. Constant-Q scans were performed with an exposure time $\sim$20 s per energy point for the single crystal and $\sim$60 s for the polycrystal (non-textured, about 1 mm thick). Measurements were performed at room temperature in transmission geometry. Eight analyzers operated simultaneously, thus particularly increasing the efficiency of experiment on the polycrystalline material, for which the Q-range from $\sim$5 to $\sim$65 nm^{-1} was covered by 6 spectrometer settings.

3. Calculations

Lattice dynamical calculations were performed with the density functional perturbation theory approach implemented in CASTEP [20]. The local density approximation was employed and the norm conserving pseudopotentials were taken from the CASTEP data base. After convergence studies the kinetic energy cut-off was set to 1000 eV. Lattice parameters were fixed to $a = 4.913$ Å and $c = 5.4052$ Å, and only internal parameters were optimised. A $7 \times 7 \times 6$ Monkhorst Pack grid was used for the electronic Brillouin zone integrals. As our lattice parameters and the pseudopotentials are very similar to those employed by Refson *et al.* (2006), the phonon dispersion curves obtained here are very similar to those in the earlier study.

For the simulation of the IXS powder data and TDS patterns phonon frequencies and eigenvectors were calculated by Fourier interpolation on a mesh with a step of 0.025 r.l.u. in the irreducible part of the Brillouin zone, shifted by 0.0125 r.l.u. away from high symmetry directions. Directional averaging was performed over a 40×40 polar mesh ($^1/_{12}$ of sphere) for momentum transfers inside the Brillouin zone centered around (000); the mesh size was progressively increased with Q. While the introduction of an orientation distribution function to the sampling procedure is straightforward [21], it was unnecessary in this particular case.

TDS intensity calculations followed the well-established formalism [22, 23] with anisotropic Debye-Waller factors derived from the lattice dynamics model as described below.

For the prediction of scattering intensities of individual phonon branches the CASTEP code output was employed as an input to scripts operating under Mathcad© which allow computing the dynamical structure factor, $S(Q, \omega)$, for any configuration, using a standard formalism [24]. The availability of the computed $S(Q, \omega)$ permits, prior to the experiment, to localize the Brillouin zones providing the highest intensity and the best contrast for a given phonon, and trace the intensity maps.

4. Results and discussion

In the following discussion we assume the validity of both (quasi)harmonic and adiabatic approximations. In that particular case the dynamical matrix $D(\boldsymbol{q})$, being the Fourier transform of the force matrix, provides the complete description of lattice dynamics of crystal. We will use the following notations: $\omega_j(\boldsymbol{q}) = \hbar^{-1}E_j(\boldsymbol{q})$ – frequency of mode j at reduced momentum transfer $\boldsymbol{q} = \boldsymbol{Q} - \boldsymbol{\tau}$; $\boldsymbol{\sigma}_d^j$ – d-site projected component of $3N$-dimensional normalized eigenvector of the phonon mode j defined in periodic notations $\boldsymbol{\sigma}^j(\boldsymbol{q} + \boldsymbol{\tau}) = \boldsymbol{\sigma}^j(\boldsymbol{q})$, where $\boldsymbol{\tau}$ is an arbitrary reciprocal lattice vector; $f_d(\boldsymbol{Q})$ – atomic scattering factor of atom d with mass M_d and Debye-Waller factor $W_d(\boldsymbol{Q})$ at the position $\boldsymbol{r}_d$; k_B – Boltzmann's constant; T – temperature. $\omega_j^2(\boldsymbol{q})$ are eigenvalues and $\boldsymbol{\sigma}^j(\boldsymbol{q})$ are eigenvectors of the dynamical matrix $D(\boldsymbol{q})$.

4.1 Vibrational density of states

The quartz vibrational density-of-states (VDOS) was obtained within the incoherent approximation [25] by summing the powder IXS spectra taken in the range of $\sim$40–65 nm^{-1} and following the data treatment previously established for nuclear inelastic scattering (absorption) [26] and successfully transferred to IXS [27]. Strictly speaking, in such a way we obtain not the true VDOS, but the generalized one:

$$\tilde{g}(E) = \sum_n \frac{G_n(E)}{M_n} \cdot f_n^2 \qquad (1)$$

where $G_n(E) = \sum_{\boldsymbol{Q},j} |\sigma_n(\boldsymbol{Q},j)|^2 \, \delta(E - E_{\boldsymbol{Q},j})$ are the partial densities of states for the atoms of type n. For the particu-

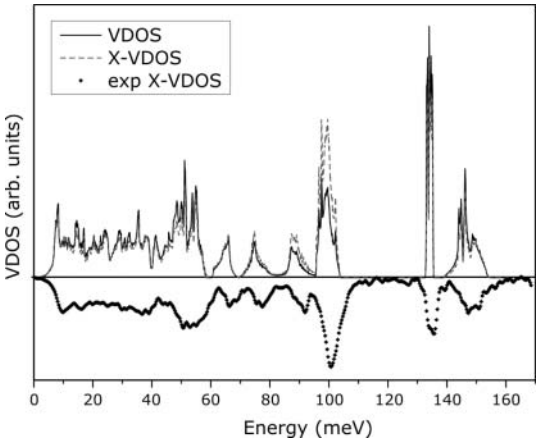

Fig. 1. Experimental X-VDOS of α-quartz (room temperature) compared to the calculated X-VDOS and the true VDOS. The areas underneath the curves are normalized to the same surface.

lar case of α-quartz we can demonstrate by direct calculation (see upper part of Fig. 1) that the generalized X-VDOS and the true VDOS are very similar below $\sim$85 meV. Thus, the VDOS extracted from the experimental data (see lower part of Fig. 1) practically coincides with the true one in this range. The comparison of the calculated and experimental VDOS shows a very reasonable agreement. We note that experimental energies below the gap at $\sim$105–130 meV are systematically slightly higher (Fig. 1). The same tendency is evidenced by the comparison of experimental and calculated phonon dispersion (Fig. 2).

Close inspection of Fig. 2 gives rise to the question, which point/area in the Brillouin zone corresponds to the first peak of the density of states (main peak of the scattering function) at $\sim$9.8 meV. Here the necessary condition

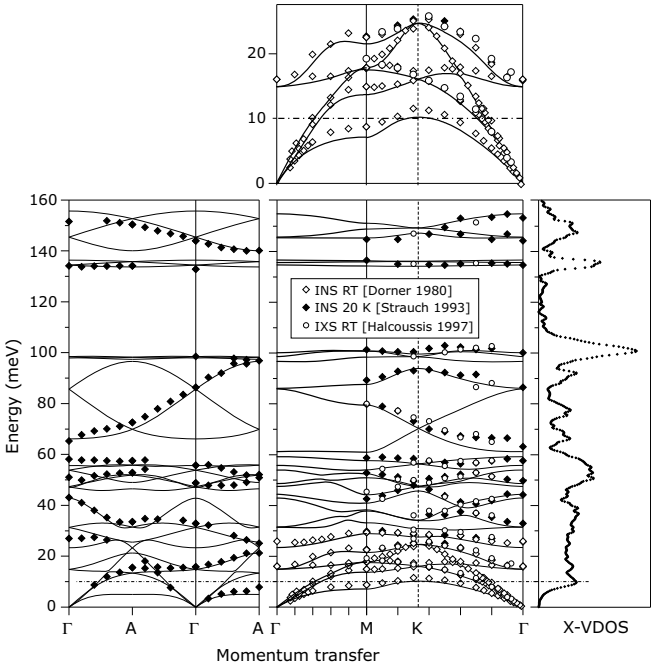

Fig. 2. Experimental phonon dispersion of α-quartz (Dorner *et al.* (1980), Strauch and Dorner (1993), Halcoussis (1997)) in comparison with dispersion curves obtained from *ab initio* calculations and experimental X-VDOS. An enlargement of dispersion curves along the Γ-*M*-*K*-Γ directions is shown for clarity.

for the existence of a VDOS peak is the existence of a van Hove singularity, namely a saddle point on the dispersion surface [28]. Phonons at none of the high symmetry points, saddle points or not, have energies corresponding to the energy of this peak; this is also true for the calculations where all the features of interest are slightly shifted towards lower energy.

4.2 Wide-angle powder IXS

The reduction of a number of IXS spectra to one incoherently approximated VDOS obviously reduces the initial information content. This shortcoming can be overcome by exploring a large Q-range, from the low Q-limit to the VDOS limit, especially where the spectral shape varies with momentum transfer due to – though relaxed – selection rules. Thus, additional constraints beyond the VDOS are provided for the lattice dynamics modeling [21, 29].

Representative experimental data obtained from the powder measurements in Q range from 5 to 65 nm^{-1} are shown in Fig. 3, where they are compared to the predicted values obtained from the DFT calculations. The agreement between the two data sets in terms of the spectral shape is good, while the same tendency as for the VDOS and single crystal phonon dispersion is observed: calculated energies below approximately 110 meV are underestimated. In this comparison no multiphonon contributions have been taken into account as no sharp features are expected to result from them.

Contrary to the example of stishovite [29], the polycrystalline spectra are not structured enough to serve as a definitely discriminating test for the calculation, so they must be completed by single crystal studies.

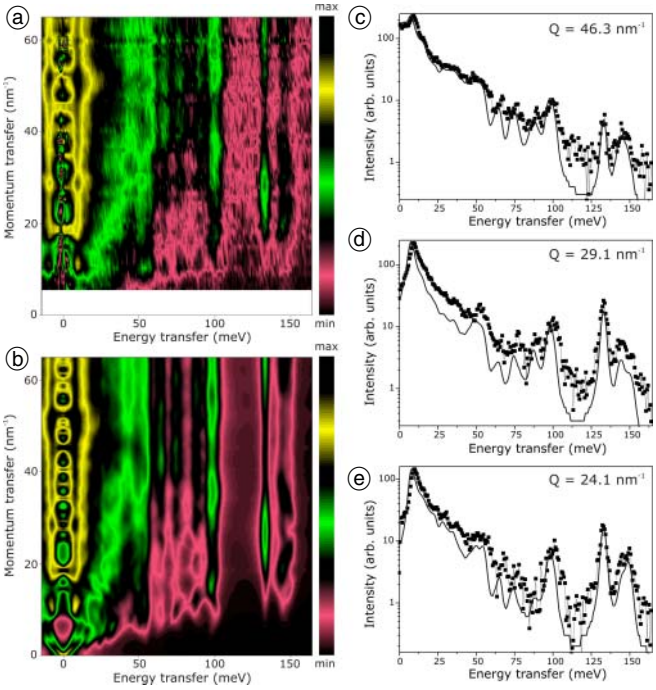

Fig. 3. Powder IXS spectra of α-quartz at room temperature: (**a**) experimental (E-Q) intensity map (log scale); (**b**) calculated (E-Q) intensity map (log scale); (**c**)–(**e**) comparison of individual experimental (black squares) and corresponding calculated (solid lines) spectra. The experimental intensity is rescaled after subtraction of the elastic line (color online). ΔQ for each spectrum corresponds to $\sim$0.25 nm^{-1}.

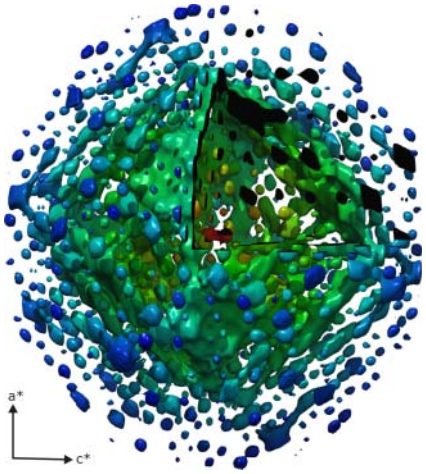

Fig. 4. Experimental isosurface of TDS intensity in α-quartz (room temperature). The color scale indicates the distance from the (000) node. One octant is removed to show the internal structure of isosurface (color online).

4.3 Thermal diffuse scattering

Inspection of the IXS spectra reveals that diffuse scattering in α-quartz is exclusively inelastic. It has a quite complex distribution in 3D space (see Fig. 4), and intense features can be readily identified outside high symmetry directions.

If we limit our considerations to high-symmetry *planes*, we can indeed identify numerous features (Fig. 5a–c), *i.e.* streaks propagating along Γ-M, which are more intense in transverse geometry (denoted by arrows in Fig. 5a), sharp inclined lines propagating along the ⟨101⟩ direction, again in transverse geometry (denoted by arrows in Fig. 5b), lines close to the ⟨112⟩ directions (arrows in Fig. 5c), and many others. Intuitively, they could be attributed to the softening of specific phonon branches, but as we will discuss in more detail below, this is not necessarily the case. Decisive conclusions for the relatively complex α-quartz structure can be made only with the support of a full lattice dynamics model. *Ab initio* calculated TDS patterns are shown in Fig. 5d–f. The convincing resemblance of experimental and calculated images reinforces the conclusions of the powder IXS experiment, namely that the model is correct not only in terms of eigenvalues (phonon energies), but also in terms of eigenvectors (phonon intensities) for *arbitrary* momentum transfers.

The only experimental eigenvector dataset which can be compared to the present calculation are results obtained by inelastic neutron scattering for the *M* point [13]. As seen from Table 1, for the lowest mode practically a one-to-one correspondence is found. The deviations for the second mode are slightly larger; this can be attributed to its known strong temperature dependency, which is not taken into account in our athermal calculations. The discrepancies concerning the sign of displacements are due to the different choice of the elementary unit cell.

4.4 Single crystal IXS

Single crystal IXS can be considered as the ultimate test of lattice dynamical models, as both energy transfer and

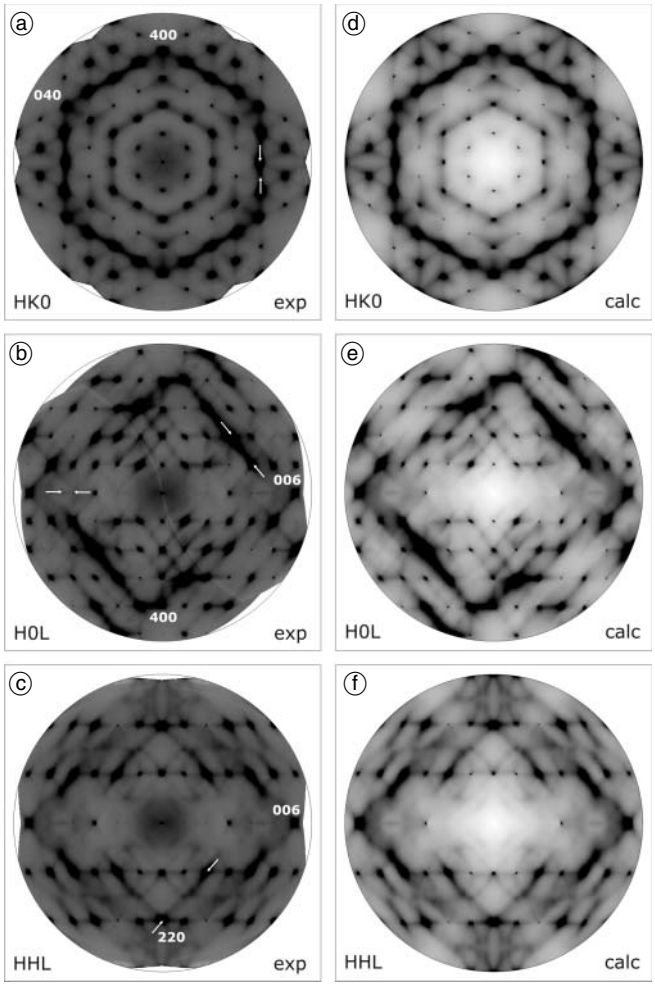

Fig. 5. Experimental (room temperature) and calculated TDS patterns of α-quartz in high-symmetry reciprocal space sections *HK*0, *H0L* and *HHL*. Experimental artifacts due to non-uniform absorption are visible. White arrows denote the sections for which IXS (*E*-*Q*) maps were recorded.

the momentum transfer vector are well-defined entities. Here, we present only a limited number of examples we found more illustrative than others. The map in Fig. 6a, seemingly without regular evolution of mode intensity and number of visible modes, traced for the ⟨112⟩ direction along the pronounced TDS feature (arrows in Fig. 5c), is in good agreement with the calculation (Fig. 6c), and the smooth diffuse line appears to be a result of the superposition of *many* phonon branches with corresponding scattered intensity transfer between them. The isolated diffuse line propagating along ⟨001⟩ in purely longitudinal geometry (horizontal arrows in Fig. 5b) was found, quite counterintuitive, to originate from the transverse acoustic (TA) phonon (Figs. 6b and d) – while the label "transverse" loses its meaning rapidly when going away from the Γ point. Two more theoretical intensity maps are presented in Fig. 6 without their experimental counterparts: Fig. 6e illustrates the domination of one "TA" phonon in the Γ-M streaks (see arrows in Fig. 5a), and Fig. 6f shows the internal structure of the strongest diffuse lines propagating along ⟨101⟩ (inclined arrows in Fig. 5b).

Table 1. Comparison of observed [13] and calculated components of the normalized eigenvectors for the two lowest *M*-point modes of α-quartz.

Atom		573 K [13] 7.8 meV	theory 7.1 meV	573 K [13] 12.1 meV	theory 13.5 meV
Si1	*x*	0	0.005	0	−0.012
	y	−0.085(17)	−0.073	0.051(41)	−0.074
	z	0.231(30)	0.222	−0.038(64)	0.056
Si2	*x*	−0.352(19)	−0.325	0.231(45)	−0.219
	y	0.135(14)	0.15	0.045(33)	−0.086
	z	0.021(22)	0.011	−0.105(67)	0.079
Si3	*x*	0.352(19)	−0.325	−0.231(45)	−0.219
	y	0.135(14)	−0.15	0.045(33)	0.085
	z	0.021(22)	−0.011	−0.105(67)	−0.075
O1	*x*	−0.261(13)	−0.291	−0.152(28)	0.148
	y	−0.275(9)	0.29	−0.121(19)	−0.124
	z	0.150(13)	−0.161	0.106(29)	0.081
O2	*x*	−0.253(16)	−0.224	0.427(23)	−0.416
	y	0.064(12)	0.075	0.061(22)	−0.127
	z	0.066(17)	0.078	0.356(39)	−0.399
O3	*x*	−0.163(11)	−0.17	−0.093(25)	0.115
	y	0.174(8)	−0.173	0.189(15)	0.149
	z	0.178(10)	−0.171	−0.159(26)	−0.083
O4	*x*	0.163(11)	−0.17	0.093(25)	0.107
	y	0.174(8)	0.173	0.189(15)	−0.149
	z	0.178(11)	0.171	−0.159(26)	0.085
O5	*x*	0.253(16)	−0.225	−0.427(23)	−0.417
	y	0.064(12)	−0.076	0.061(22)	0.122
	z	0.066(17)	−0.079	0.356(39)	0.403
O6	*x*	0.261(13)	−0.291	0.152(28)	0.146
	y	−0.275(9)	−0.29	−0.121(19)	0.123
	z	0.150(13)	0.162	0.106(29)	−0.078

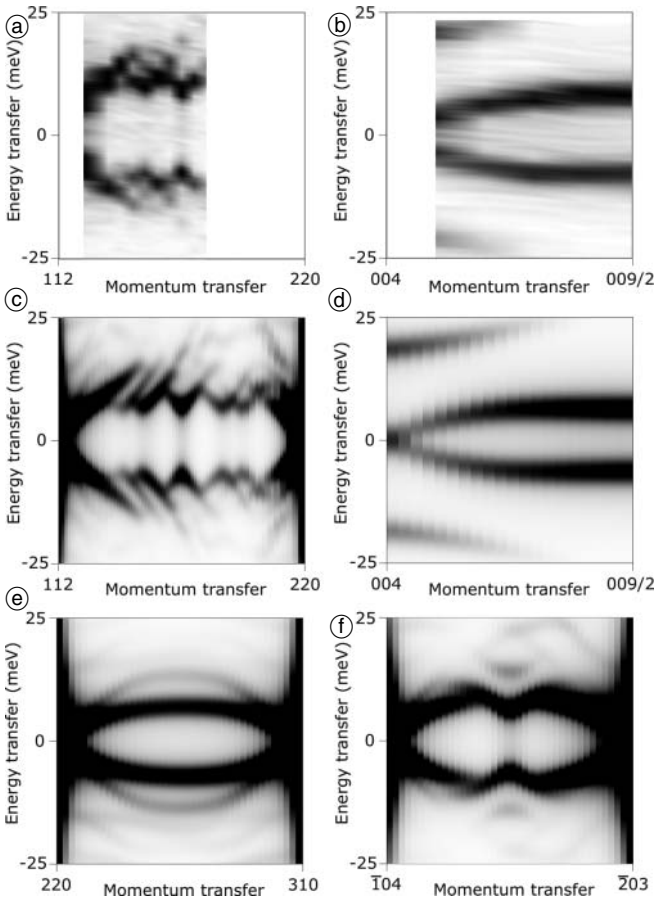

Fig. 6. Experimental (**a**), (**b**) and calculated (**c**)–(**f**) (*E*-*Q*) intensity maps for α-quartz (room temperature). Panel (**a**) can be directly compared to (**c**), and panel (**b**) can be compared to (**d**).

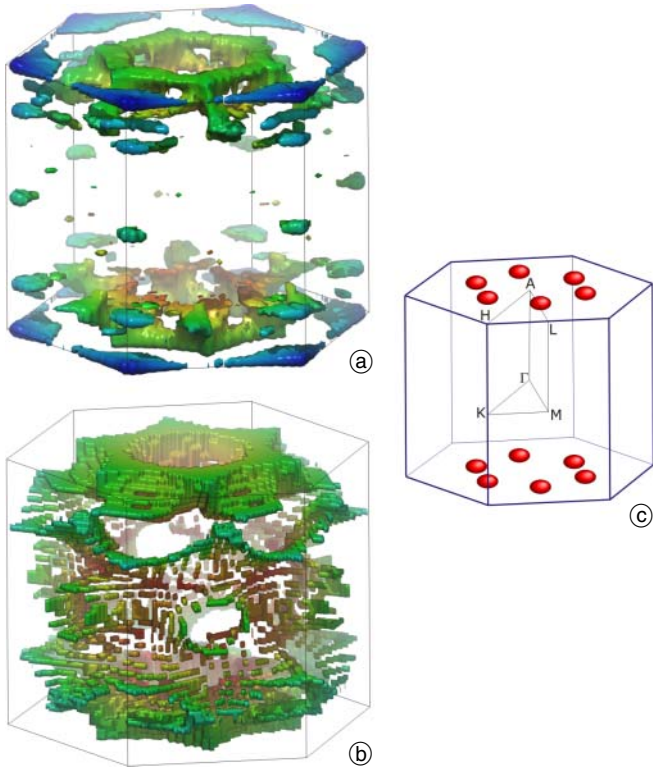

Fig. 7. Lowest α-quartz phonon mode: (**a**) isosurface of VDOS contribution estimate $|\nabla\omega|^{-1}$ and (**b**) $\boldsymbol{q}$ points with a frequency of 66 ± 1 cm^{-1}, (**c**) Brillouin zone and identified area of interest around $\{^1/_4\ 0\ ^1/_2\}$ (color online).

4.5 Van Hove singularity: *ab initio* and single crystal IXS

Following the convincing validation of the lattice dynamics model we now discuss the first peak in the VDOS and the associated localization of a van Hove singularity in reciprocal space. If only a search with an energy window ($\omega = \omega_C \pm \Delta$) is performed, too many accidental coincidences make the result difficult to interpret. On the other side, if one just considers areas which contribute most to the VDOS, based on the minimum gradient criterion ($|\nabla\omega| \to 0$) [28], features with a wrong energy could be selected. In fact, it turned out that the simultaneous use of both filters per phonon branch represents the best solution. As can be seen from the comparison of Fig. 7a and b, the common region for the two filters is located close to ($^1/_4\ 0\ ^1/_2$).

A subsequent IXS experiment fully confirmed the existence of a saddle point in this region: maxima in two orthogonal directions and a minimum in the third direction (see Fig. 8). The energy of the phonon at the saddle point is ∼9.5 meV, thus coinciding closely with the VDOS peak position of ∼9.8 meV.

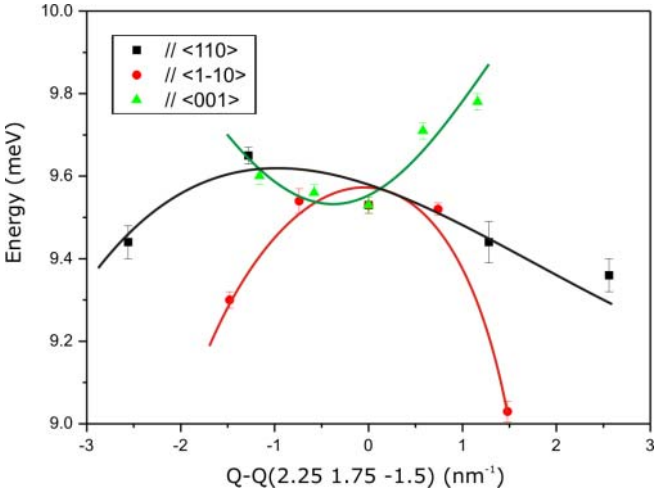

Fig. 8. Room temperature dispersion of the lowest phonon branch of α-quartz in the proximity of the (2.25 1.75 −1.5) point, corresponding to (0.25 0 0.5) in the reduced Brillouin zone scheme. Lines are guides to the eye in order to underline the saddle point nature of the singularity (color online).

The displacement pattern for ($^1/_4$ 0 $^1/_2$) shown in Fig. 9 is quite complex. The largest displacement is seen for oxygen atoms; tetrahedron deformation and tilt take place simultaneously while silicon displacement remains small. From the quartz data only we cannot conclude if some features of this pattern are linked to the boson peak in silica, the amorphous form of quartz. Detailed investigations of the other SiO_2 polymorphs (coesite, tridimite, cristobalite) containing the same SiO_4 tetrahedral units might shed further light.

4.6 Debye-Waller factors

The established lattice dynamics model allows us to calculate the thermal contribution to the Debye-Waller factors using the standard formalism

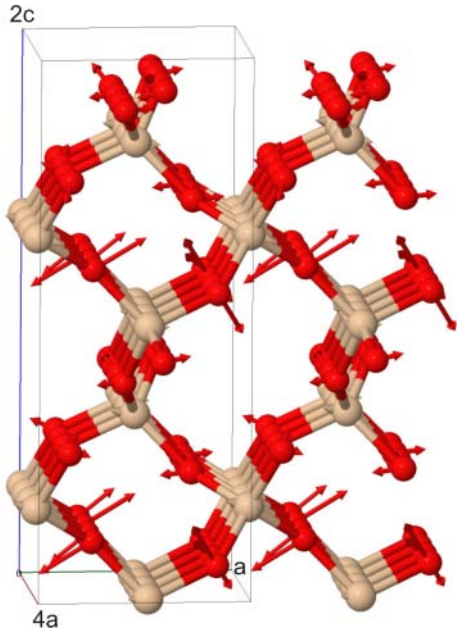

Fig. 9. Displacement pattern for the lowest phonon mode in α-quartz at ($^1/_4$ 0 $^1/_2$), represented in a 4 × 1 × 2 supercell (color online). Jmol visualisation [30].

$$W_d(\boldsymbol{Q}) = \frac{1}{2}\langle\{\boldsymbol{Q}\boldsymbol{u}_d\}^2\rangle = \frac{\hbar V}{32NM_d\pi^3}\sum_j \int_{BZ} \omega_j^{-1}|\boldsymbol{Q}\sigma_d^j(\boldsymbol{q})|^2 \times \coth\left(\hbar\omega_j/2k_BT\right)\mathrm{d}V_{\boldsymbol{q}} = \boldsymbol{Q}^T\boldsymbol{U}_d\boldsymbol{Q}\,. \quad (2)$$

Thus, the amplitude matrix will be expressed as

$$\boldsymbol{U}_d = \frac{\hbar V}{32NM_d\pi^3}\sum_j \int_{BZ} \omega_j^{-1}\boldsymbol{\sigma}_d^j(\boldsymbol{q})\otimes\boldsymbol{\sigma}_d^j(\boldsymbol{q})^{*T} \times \coth\left(\hbar\omega_j/2k_BT\right)\mathrm{d}V_{\boldsymbol{q}}\,. \quad (3)$$

Otherwise, the generalized $3N$-dimensional amplitude matrix $\boldsymbol{U}^{3N}$, containing $\boldsymbol{U}_d$ submatrices on the main diagonal, can be written *via* Born's S-matrix

$$S(\boldsymbol{q}) = \frac{\hbar}{2\sqrt{\boldsymbol{D}(\boldsymbol{q})}}\coth\left(\frac{\hbar\sqrt{\boldsymbol{D}(\boldsymbol{q})}}{2kT}\right) \quad (4)$$

as

$$\boldsymbol{U}^{3N} = \boldsymbol{m}^{-1}\left(\frac{V}{16N\pi^3}\int_{BZ} S(\boldsymbol{q})\,\mathrm{d}V_q\right)\boldsymbol{m}^{-1}\,, \quad (5)$$

where $m_{ij} = \delta_{ij}M_{[i/3]}$

In the high-temperature limit $\left(\frac{\hbar}{kT}\right)^2\|D(\boldsymbol{q})\| \ll 1$ this expression reduces to

$$\boldsymbol{U}^{3N} = \frac{k_BTV}{16N\pi^3}\,\boldsymbol{m}^{-1}\left(\int_{BZ}\boldsymbol{D}^{-1}(\boldsymbol{q})\,\mathrm{d}V_q\right)\boldsymbol{m}^{-1}\,, \quad (6)$$

coinciding with the previous result [31] within a factor 2.

The thus calculated Debye-Waller factors are compared with experiment in Table 2. The component-by-component comparison is extended by the comparison of tensor invariants like $|U|$, tr (U) and tr (U^2), which might be even more informative. It can be seen, that our calculations are in reasonable agreement with single crystal neutron diffraction data, in particular for silicon atoms. A more detailed investigation is necessary to elucidate the nature of the apparent deviations.

5. Conclusions

For α-quartz we successfully used an approach based on combining coherent wide-angle IXS from polycrystalline sample with TDS from single crystal and first principle lattice dynamics calculations. In both cases the experimental data naturally contain information for arbitrary momentum transfers as well as eigenvalues and eigenvectors of the dynamical matrix, subject to orientational integration (for polycrystalline IXS) or to energy integration (for TDS). While the lattice dynamics information in terms of a simultaneous retrieval of phonon energy and momentum is not directly extractable, the two complementary data sets provide highly discriminating constraints to lattice dynamical models, and hence can be used to evaluate such models. An ultimate cross-check in our case was provided

Table 2. Comparison of experimental and calculated anisotropic thermal parameters for α-quartz at room temperature. U_{ij} are given in 10^{-4} Å^2, $|U|$ in 10^{-7} Å^6, tr (U^2) in 10^{-7} Å^4.

	Si				O			
	[32][a]	[33][b]	[34][c]	this work	[32][a]	[33][b]	[34][c]	this work
U_{11}	66(1)	56(2)	71	45	156(4)	137(2)	150	92
U_{22}	51(1)	39(2)	53	51	115(3)	93(2)	113	94
U_{33}	60(1)	52(2)	65	44	119(3)	109(1)	118	91
U_{12}	26(1)	19(1)	26	4	92(3)	78(1)	88	6
U_{13}	−1(1)	−3(1)	−1	1	−29(3)	−30(1)	−32	7
U_{23}	−3(1)	−6(2)	−1	0	−46(2)	−48(1)	−44	5
$\|U\|$	161	93	201	100	946	551	928	784
tr (U)	177	147	189	139	390	339	381	278
tr (U^2)	12	8	8	7	75	58	71	26

a: Single crystal X-ray diffraction
b: Single crystal neutron diffraction
c: Calculation: empirical potentials

by single crystal IXS for selected momentum transfers. Once the reliability of a lattice dynamical model is established in this way, it can be used to provide insight not readily available from the limited available experimental data sets. An important point here is that the lattice dynamical model is not evaluated directly against phonon dispersion curves, but against data which are much easier and faster to obtain than conventional single crystal inelastic scattering data.

To conclude, we have shown that thermal diffuse scattering experiments can serve as a rigorous benchmark for parameter-free model calculations even for relatively complex structures, in particular if they are complemented with inelastic scattering techniques on powder, single crystals or both of them. Once the validity of the model is established, it then can be used to gain valuable insight into the dynamical properties of materials, often in a more meaningful way than from phonon dispersion curves or phonon-density-of-states alone.

In the particular case of α-quartz a number of observations have been made: i) the intense TDS features are not necessarily related to individual soft phonon branches; ii) the soft branches are not necessarily associated with visible VDOS singularities; iii) intuitively evident selection rules in complex structures can fail even for the acoustic phonons. We were furthermore able to identify the area in the Brillouin zone close to ($^1/_4$ 0 $^1/_2$) as the one responsible for the first VDOS peak.

As a remark of general interest, we note that reporting results of *ab initio* calculations as phonon dispersion curves leaves the major part of useful information inaccessible to the reader. We suggest that the interpolation parameters for constructing the dynamical matrices for arbitrary points in reciprocal space should be requested as supplementary material.

References

[1] Dolino, G.; Berge, B.; Vallade, M.; Moussa, F.: Origin of the incommensurate phase of quartz: I. Inelastic neutron scattering study of the high temperature β phase of quartz. J. Phys. I France **2** (1992) 1461–1480.

[2] Vallade, M.; Berge, B.; Dolino, G.: Origin of the incommensurate phase of quartz: II. Interpretation of inelastic neutron scattering data. J. Phys. I France **2** (1992) 1481–1495.

[3] Rudnick, R. L.; Gao, S.: Composition of the Continental Crust. In The Crust (ed. R. L. Rudnick) Vol. 3, P. 1–64 of Treatise on Geochemistry (eds. H. D. Holland and K. K. Turekian), Elsevier-Pergamon, Oxford (2003).

[4] Baldi, G.; Fontana, A.; Monaco, G.; Orsingher, L.; Rols, S.; Rossi, F.; Ruta, B.: Connection between Boson Peak and Elastic Properties in Silicate Glasses. Phys. Rev. Lett. **102** (2009) 195502-1-4.

[5] Rufflé, B.; Parshin, D. A.; Courtens, E.; Vacher, R.: Boson Peak and its Relation to Acoustic Attenuation in Glasses. Phys. Rev. Lett. **100** (2008) 015501-1-4.

[6] Calderon, E.; Gauthier, M.; Decremps, F.; Hamel, G.; Syfosse G.; Polian, A.: Complete determination of the elastic moduli of α-quartz under hydrostatic pressure up to 1 GPa: an ultrasonic study. J. Phys.: Condens. Matter **19** (2007) 436228-1-13.

[7] Krishnan, R. S.: Raman Spectrum of Quartz. Nature **155** (1945) 452.

[8] Ichikawa, S.; Suda, J.; Sato T.; Suzuki Y.: Lattice dynamics and temperature dependence of the first-order Raman spectra for α-SiO_2 crystals. J. Raman Spectrosc. **34** (2003) 135–141.

[9] Spitzer, W. G.; Kleinman, D. A.: Infrared Lattice Bands of Quartz. Phys. Rev. **121** (1961) 1324–1335.

[10] Dorner, B.; Grimm H.; Rzany, H.: Phonon dispersion branches in α-quartz. J. Phys. C: Solid St. Phys. **13** (1980) 6607–6612.

[11] Strauch D.; Dorner, B.: Lattice dynamics of alpha-quartz. I. Experiment. J. Phys.: Condens. Matter **5** (1993) 6149–6154.

[12] Halcoussis, Ch.: Ph.D. Thesis, Rostock University (1997).

[13] Boysen, H.; Dorner, B.; Frey, F.; Grimm, H.: Dynamic structure determination for two interacting modes at the *M*-point in α- and β-quartz by inelastic neutron scattering. J. Phys. C: Solid St. Phys. **13** (1980) 6127–6146.

[14] Refson, K.; Tulip P. R.; Clark, S. J.: Variational density-functional perturbation theory for dielectrics and lattice dynamics Phys. Rev. B**73** (2006) 155114-1-12.

[15] Brönnimann, C.; Eikenberry, E. F.; Henrich, B.; Horisberger, R.; Hülsen, G.; Pohl, E.; Schmitt, B.; Schulze-Briese, C.; Suzuki, M.; Tomizaki, T.; Toyokawa H.; Wagner, A.: The PILATUS 1M detector. J. Synchrotron. Radiat. **13** (2006) 120–130.

[16] Oxford Diffraction Ltd.

[17] Pettersen, E. F.; Goddard, T. D.; Huang, C. C.; Couch, G. S.; Greenblatt, D. M.; Meng, E. C.; Ferrin, T. E.: UCSF chimera – A visualization system for exploratory research and analysis. J. Comput. Chem. **25** (2005) 1605–1612.

[18] http://www.povray.org

[19] Krisch M.; Sette, F.: Inelastic X-ray Scattering from Phonons. Light Scattering in Solids, Novel Materials and Techniques, Topics in Applied Physics 108, Springer-Verlag Berlin Heidelberg (2007).

[20] Clark, S. J.; Segall, M. D.; Pickard, C. J.; Hasnip, P. J.; Probert, M. J.; Refson, K.; Payne, M. C.: First principles methods using CASTEP. Zeitschrift für Kristallographie **220** (2005) 567–570.
[21] Fischer, I.; Bosak, A.; Krisch, M.: Single-crystal lattice dynamics derived from polycrystalline inelastic X-ray scattering spectra. Phys. Rev. B**79** (2009) 134302-1-8.
[22] Xu, R.; Chiang, C.: Determination of phonon dispersion relations by X-ray thermal diffuse scattering. Z. Kristallogr. **220** (2005) 1009–1016.
[23] Bosak, A.; Chernyshov, D.: On model-free reconstruction of lattice dynamics from thermal diffuse scattering. Acta Cryst. A**64** (2008) 598–600.
[24] Burkel, E.: Phonon spectroscopy by inelastic X-ray scattering. Rep. Prog. Phys. **63** (2000) 171–232.
[25] Bredov, M. M.; Kotov, B. A.; Okuneva, N. M.; Oskotskii, V. S.; Shakh-Budagov, A. L.: Possibility of Measuring the Thermal Vibration Spectrum $g(\omega)$ using Coherent Inelastic Neutron Scattering from a Polycrystalline Sample. Sov. Phys. Solid State **9** (1967) 214–218.
[26] Kohn V. G.; Chumakov, A. I.: DOS: Evaluation of phonon density of states from nuclear resonant inelastic absorption. Hyperfine Interactions **125** (2000) 205–221.
[27] Bosak, A.; Krisch, M.: Phonon density of states probed by inelastic X-ray scattering. Phys. Rev. B**72** (2005) 224305-1-9.
[28] Van Hove, L.: The Occurrence of Singularities in the Elastic Frequency Distribution of a Crystal. Phys. Rev. **89** (1953) 1189–1193.
[29] Bosak, A.; Fischer, I.; Krisch, M.; Brazhkin, V.; Dyuzheva, T.; Winkler, B.; Wilson, D.; Weidner, D.; Refson, K.; Milman, V.: Lattice dynamics of stishovite from powder inelastic X-ray scattering. Geophys. Res. Lett. **36** (2009) L19309-1-6.
[30] Jmol: an open-source Java viewer for chemical structures in 3D. http://www.jmol.org/
[31] Scheringer, C.: On the interpretation of anisotropic temperature factors. Acta Cryst. A**28** (1972) 512–515.
[32] Lepage, Y.; Donnay, G.: Refinement of the crystal structure of low-quartz. Acta Cryst. B**32** (1976) 2456–2459.
[33] Wright, A. F.: Lehmann, M. S.: The Structure of Quartz at 25 and 590 °C Determined by Neutron Diffraction. J. Solid State Chem. **36** (1981) 371–380.
[34] Pilati, T.; Demartin, F.; Gramaccioli, C. M.: Thermal parameters for *a*-quartz: a lattice-dynamical calculation. Acta Cryst. B**50** (1994) 544–549.